Int J Adv Manuf Technol (2017) 91:1129–1143
DOI 10.1007/s00170-016-9812-9

ORIGINAL ARTICLE

Numerical study of the effect of laser-arc distance on laser energy coupling in pulsed Nd: YAG laser/TIG hybrid welding

Jie Ning[1] · Lin-Jie Zhang[1] · Suck-Joo Na[2] · Xian-Qing Yin[1] · Jing Niu[1] · Jian-Xun Zhang[1] · Huan-Ran Wang[3]

Received: 6 August 2016 / Accepted: 21 November 2016 / Published online: 2 December 2016

Abstract A three-dimensional (3-d) computational fluid dynamics (CFD) based model in which a ray-tracing algorithm was combined with the volume of fluid (VOF) method was used to simulate a pulsed Nd: YAG laser /tungsten inert gas (TIG) hybrid welding process. The calculated weld cross sections in pure laser welding and hybrid welding process were validated by the experimental results, respectively. Then, the variations of keyhole shape and laser energy coupling behaviour in the laser-arc hybrid welding process were calculated at three different laser-arc distances. It was found that the laser-arc distance would affected the shape of keyhole generated in the laser-arc hybrid welding process, thus influencing the laser energy coupling efficiency. In the initial stage of each laser pulse, small laser-arc distances favoured the generation of keyholes and multiple reflections of laser beam within keyhole. However, as the laser irradiation time increased, the smaller the laser-arc distance, the more liquid metal were found around the keyholes, which was more favourable to the expansion of keyhole in radial direction. As a result, the aspect ratio of keyhole, the reflection time of laser beams in keyhole, and the laser energy absorbed by keyhole wall decreased. Given that the interaction between laser and arc was neglected, the maximum keyhole depth increased with reducing laser-arc distances, while the total laser energy coupling efficiency decreased as the laser-arc distance was reduced.

Keywords Pulsed Nd:YAG laser/TIG hybrid welding · Laser-arc distance · Laser energy coupling behaviour · CFD-based simulation

1 Introduction

The combination of arc and laser welding offered advantages such as greater joint fit-up tolerance, improved gap bridging ability, higher melting efficiency, enhanced productivity, and larger weldable material thickness. In addition, reduced susceptibility to pores and cracks and additional flexibility in control over seam geometry were also found [1–11]. The investigation about laser energy coupling and heat transfer efficiency has drawn many researchers' attention. Hu et al. [12] studied the synergetic effects of hybrid laser/arc welding and found that a much higher local current density and focused power input in the area of laser impact which can cause higher melting efficiency. The results of Kozakov et al. [13]showed that about 8% of the power is absorbed for the laser with 100 W set value and about 16% for the laser with 367 W when the laser passes the arc axis for an arc current of 120 A. Furthermore, Fuerschbach et al. [14, 15] used thermometer to measure the heat transfer efficiency of YAG laser spot welding of stainless steel and an empirical relationship between coupling coefficient and laser power was proposed. Their results showed that beam intensity had an obvious effect on the energy transfer efficiency during, while there were no correlations with energy transfer efficiency was found for the fusion zone depth-to-width ratio or the travel speed. In addition, Jouvard [16] compared the mean absorption during a pulse with a measurement using a differential microcalorimeter and found that the absorption increases strongly

✉ Lin-Jie Zhang
zhanglinjie@mail.xjtu.edu.cn

[1] State Key Laboratory of Mechanical Behavior for Materials, Xi'an Jiaotong University, Xi'an 710049, China

[2] Department of Mechanical Engineering, KAIST, Daehak-ro 291, Yuseong-gu, Daejeon 305-701, Republic of Korea

[3] School of Energy and Power Engineering, Xi'an Jiaotong University, Xi'an 710049, China

during the formation of the keyhole and tends towards a limit value. And the simulation results of Hu et al. [17] showed that the energy absorption efficiency rose from 42 to 59% during the keyhole forming, which was approximately linear with the depth of the keyhole. Kaplan [18] compared the laser absorption at the keyhole wall between smooth and wavy surface and the results showed that the increasing roughness could enhance the surface-integrated absorptance. Furthermore, the absorptivity trends across a wavy surface of liquid metal for five major metals, namely, Ti, Fe, Mg, Al, and Cu, and for these four high-power laser wavelengths, 10.6, 1070, 808, and 532 nm, are further generalised in Ref. [18]. It has also been reported that a pulsing laser beam reduces energy coupling by approximately 25% compared with continuous laser beam [19]. Zhang [20] took an investigation of the influence of the metal vapour from the wire end on the plasma and further on the absorption of the laser irradiation and the energy input to workpiece. Greses [21] calculated the heat loss during laser welding of low carbon steel by analysing the temperature and electron density of laser-induced plasma.

The distance between laser and arc (d_{LA}) is one of the crucial factors influencing laser-arc hybrid welding processes, and its influence on the laser-arc hybrid welding process has been studied by many researchers. Investigations by Matsuda et al. showed that the welding results of laser-arc hybrid welding strongly depend on d_{LA} [22]. They found that the maximum value of penetration was achieved at the smallest possible distance between the laser beam axis and electrode tip. They believed that this phenomenon was mainly caused by the fact that the laser beam, when set at small distances from the tip of the welding electrode, struck the deepest part of the melt pool surface, which was commonly depressed by the arc forces. Katayama et al. investigated the effect of d_{LA} on weld depth and found that it exerted a significant effect on not only the weld penetration but also the weld geometry [23]. Liu et al. found that in tungsten inert gas (TIG)-laser hybrid welding processes, the welding penetration depth increased first and then decreased with increasing d_{LA} [24]. This suggested that the horizontal distance L between the deepest point of depressed molten pool surface and the TIG electrode increased with the increasing of arc current. Besides, the greatest penetration depth could be formed when the laser acted at the deepest point of the arc crater. Andersen et al. reported that if the coupling between laser beam and arc was too close, the arc would disturb the stability of keyhole, which then decreased the penetration [25]. In addition, if the distance was increased to such an extent that each process had its own molten pools, the penetration also decreased owing to the decrease in synergistic action. Uchiumi et al. showed that in YAG laser-pulsed metal inert gas (MIG) hybrid welding at a d_{LA} of 0 mm, the laser beam irradiated flying droplets [26] and thus, the droplets blocked laser beam irradiation, which resulted in shallower weld penetration. Moradi et al. reported that a short laser-arc distance destabilised the laser-arc hybrid welding process for the drop interacts directly with the keyhole, causing additional flow disturbances [27]. Song et al. investigated the overlap weldability of magnesium alloy AZ31B sheets by a laser-arc hybrid welding process. They found that d_{LA} was a key factor affecting penetration depth and bead shape [28]. Kim et al. studied the relationship between weldability and d_{LA} in the lap welding of zinc-coated steel. They found that fewer spatters were created as d_{LA} increased [29]. Abe et al. [30] analysed the behaviour of the laser and arc plasma by means of high-speed photographs and found that the laser-induced plasma was capable of stabilising the arc plasma [30]. The strength of this stabilising effect depended on the distance between the laser beams and the arc while it disappeared at greater displacements. Ribic et al. showed that time-averaged plasma electron temperatures, electron and ion densities, electrical conductivity, and arc stability decreased with increasing d_{LA} during laser-arc hybrid welding [31]. They suggested that there was possibly an optimal heat source separation distance for a given arc current where hybrid weld penetration depth was the greatest.

CFD-based simulation has been proved to be a robust tool to quantitatively reveal the molten behaviour during welding process [32–44]. To improve understanding of laser-arc hybrid welding process, much research effort has also been devoted to numerical simulation thereof. Cho et al. simulated the hybrid plasma generated by an Nd:YAG laser and a gas tungsten arc (GTA) [45] and revealed that the plasma was concentrated in the vicinity of the laser-irradiation position and that the local temperature of the plasma was increased. Piekarska developed a three-dimensional (3-d) transient laser-arc hybrid welding model and studied the thermal phenomena in laser-arc hybrid welding [46]. Bendaoud et al. established a 3-d quasi-steady state hybrid laser/MIG welding model using equivalent heat source approach to analyse heat transfer effects in the hybrid welding of a duplex steel with a Y-shaped chamfer [47]. They reported that when laser-arc distances increased, the width of the upper part of the fusion zone increased. Cho et al. numerically studied the mixing of alloy elements in a CO_2 laser–GMA hybrid welding process and found that a relatively low content of alloying elements was observed in the low molten region. This was because the flow with its large alloying element content was pushed out by the excessive flow at the rear part of the keyhole [48]. Zhou et al. developed a mathematical model to investigate the mixing and diffusion processes in laser–MIG hybrid welding by tracing the distribution of sulphur concentrations in the fusion zone [49]. It is noted that any numerical study of the effects of laser-arc distance on laser-arc hybrid welding processes is limited. Ribic et al. used a 3-d heat transfer and fluid flow model to study the heat transfer and fluid flow in a GTA/laser hybrid welding process and found that d_{LA} significantly affected the cooling rates [50]. They suggested that hybrid weld pool penetration depth was maximised at an optimal distance between

the arc electrode and laser beam. Meanwhile, they pointed out that the cooling rate increased significantly when the heat sources were separated beyond a critical distance. However, it remains a limitation in their work that the keyhole geometry was calculated based on an energy balance on keyhole walls.

In this work, to obtain more details of the role of d_{LA} in laser-arc hybrid welding processes, pulsed Nd: YAG laser/TIG hybrid welding processes were simulated by using a computational fluid dynamics (CFD)-based model. In this model, a ray-tracing algorithm was combined with the volume of fluid (VOF) method to simulate the dynamic evolution of keyholes and their influence on laser energy coupling behaviour. Simulations of arc leading hybrid welding process were carried out for three different values of d_{LA} (i.e., 0 mm, 1.5 mm, and 2.5 mm). The influences of d_{LA} on laser energy transfer in a laser-arc hybrid welding process were discussed based on the simulation results.

2 Mathematical model

2.1 Assumptions

Those assumptions used in the simulation are listed below:

1). The molten metal was assumed to be a laminar incompressible Newtonian fluid;
2). Interaction between the laser induced plasma and the arc plasma was neglected;
3). The evaporation induced recoil pressure was governed by the Clausius–Clapeyron equation;
4). Inside a blind keyhole, the vapour velocity along the keyhole depth was assumed to increase linearly from zero velocity at the bottom of the blind keyhole to its calculated velocity at the entrance of the blind keyhole;
5). The temperature dependency of the absorption factor of metal for laser irradiation was neglected;
6). The buoyancy force was simulated by the Boussinesq approximation.

2.2 Governing equations and heat source models

2.2.1 Governing equations

The governing equations describing the melt flow and heat transfer in the molten pool were as follows:

Mass conservation equation was expressed as

$$\nabla\cdot\mathbf{v} = 0 \tag{1}$$

where $\mathbf{v}$ was the velocity vector.

The Navier–Stokes equation was represented as:

$$\frac{\partial\mathbf{v}}{\partial t} + \mathbf{v}\cdot\nabla\mathbf{v} = -\frac{1}{\rho}\nabla P + \nu\nabla^2\mathbf{v} - K\mathbf{v} + \mathbf{G} \tag{2}$$

$$K = C\frac{F_S^2}{(1-F_S)^3 + B} \tag{3}$$

where ρ was the fluid density, ν was the dynamic viscosity, P was the pressure, K was the drag coefficient in mushy zone, C was a constant reflecting the mushy zone morphology, F_S was the solid fraction, B was the positive zero taken to avoid division by zero, and G was the body acceleration due to gravity.

The energy conservation equation was:

$$\frac{\partial h}{\partial t} + \mathbf{v}\cdot\nabla h = \frac{1}{\rho}\nabla\cdot(k\nabla T) \tag{4}$$

where k was the thermal conductivity, T was the temperature, and h was the enthalpy.

The VOF equation was as follows:

$$\frac{\partial F}{\partial t} + \nabla\cdot(\mathbf{v}F) = 0 \tag{5}$$

where, F was the volume fraction of fluid.

2.2.2 Arc heat source model

The arc heat source was simulated as a surface heat flux with Gaussian distribution [6]:

Table. 1 Material properties used in simulation

Physical property	Value
Density of liquid metal ρ (kgm^{-3})	6800
Density of solid metal ρ (kgm^{-3})	7170
Thermal conductivity of liquid k_L ($Wm^{-1}\ K^{-1}$)	29
Thermal conductivity of solid k_S ($Wm^{-1}\ K^{-1}$)	27
Viscosity μ ($kgm^{-1}\ s^{-1}$)	0.007
Surface tension γ (Nm^{-1})	1.87
Surface tension gradient $d\gamma/dT$ ($Nm^{-1}\ K^{-1}$)	-4.7×10^{-4}
Specific heat of solid C_S ($Jkg^{-1}\ K^{-1}$)	730
Specific heat of liquid C_L ($Jkg^{-1}\ K^{-1}$)	760
Latent heat of fusion h_{SL} (Jkg^{-1})	2.99×10^5
Latent heat of vaporisation h_V (Jkg^{-1})	6.52×10^6
Coefficient of thermal expansion β	1.96×10^{-5}
Liquidus temperature T_L (K)	1727
Solidus temperature T_S (K)	1672
Boiling temperature T_V (K)	2900
Convection heat transfer coefficient h ($Wm^2\ K^{-1}$)	10
Emissivity ε	0.4

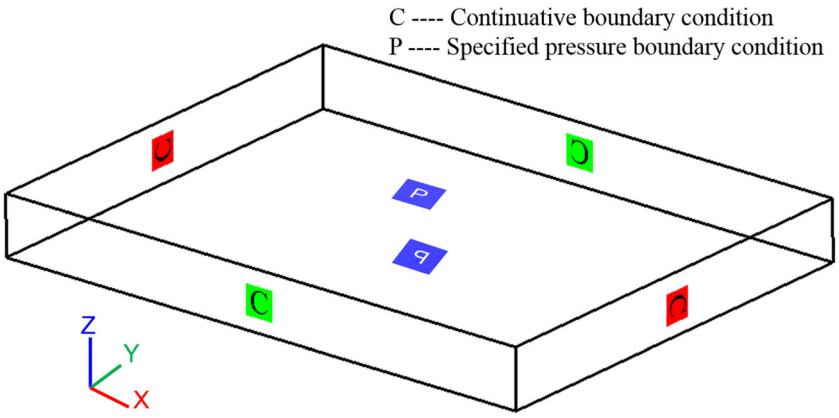

Fig. 1 The coordinate system and boundary types used in the study

$$\eta_A q_A(r) = \eta_A \frac{UI}{2\pi \cdot {r_A}^2} \exp\left(-\frac{r^2}{2{r_A}^2}\right) \tag{6}$$

where η_A was the effective coefficient of arc heat source; U and I were the voltage and current of the arc, respectively; r_A was the radius of the region heated by arc; and r was the distance between the centre of the region heated by arc and any point of the workpiece surface. The arc pressure acted on the molten pool surface also was described by a Gaussian function [7]:

$$P_A(r) = \frac{\mu_0 I^2}{4\pi \cdot {r_A}^2} \exp\left(-\frac{r^2}{2{r_A}^2}\right) \tag{7}$$

where μ_0 was the free space magnetic permeability.

The plasma drag force was acted on the surface due to impingement effect of arc plasma jet flow and it led to outward flow from the centre. To simulate the plasma drag force, the following analytical solution of the wall shear stress produced by the normal impingement of the jet on the flat surface was employed [9]:

$$\frac{\tau}{\rho_p u_0^2} \mathrm{Re}_0^{1/2} \left(\frac{H}{D}\right)^2 = g_2\left(\frac{r}{H}\right) \tag{8}$$

where τ was the shear stress; ρ_p was the density of plasma; u_0 was the initial velocity of plasma; Re_0 was the Reynolds number; H was the length of arc; D was diameter of the nozzle; r was the radius from the centre; and g_2 was a universal function.

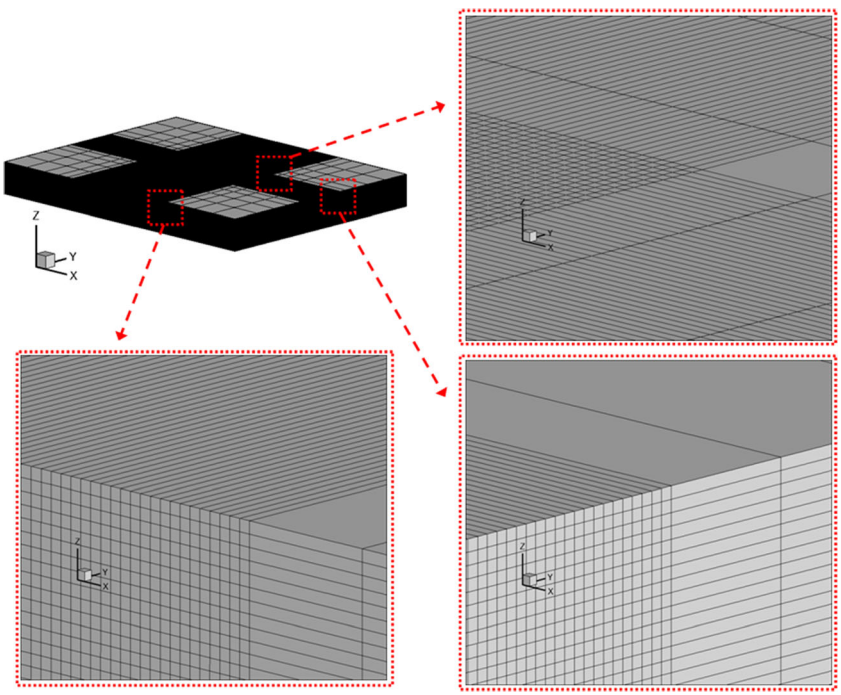

Fig. 2 The mesh used in the study

Table. 2 The detailed parameters in various welding processes

Welding procedure	Average power (W)	Pulse width (ms)	Travel speed (mm/min)	Frequency (Hz)	Defocusing distance (mm)	Arc current (A)	Arc voltage (V)	d_{LA} (mm)
Pure laser welding	350	5.5	500	20	0	–	–	–
Defocused laser welding	350	5.5	500	20	0	80	12	0
Hybrid laser-arc welding	350	5.5	500	20	0	80	12	0

2.2.3 Laser beam heat source model

Laser energy distribution on focal plane was simulated by a Gaussian function:

$$I(r) = \frac{2P_L}{{r_{f0}}^2\pi}\exp\left(-\frac{2r^2}{{r_{f0}}^2}\right) \tag{9}$$

where, P_L was the laser power and r_{f0} was the focal spot radius, as expressed by the following equation:

$$r_{f0} = \frac{2\lambda F M^2}{\pi} \tag{10}$$

where λ was the wavelength of laser irradiation; f was the focal length; and M^2 was the laser beam quality index. In this paper, the beam parameter product (BPP) was about 31 mm·mrad. The wavelength of laser irradiation (λ) was 1.06 μm. The focal length (F) was 70 mm.

The FlOW3D software was employed in present study, in which finite volume method was used to simulate the process of melt flow. The hexahedral element was adopted. The theory of the VOF method could be found elsewhere [51], so was not repeated here. A detailed introduction to the laser beam profile, the sub-model of multiple reflections within keyhole, the sub-model of recoil pressure, the sub-model of Fresnel absorption, the calculation method of the vapour velocity, the calculation method of the shear stress, and the method of calculation the impact of vapour jet on the opposite keyhole wall could be found in the previously published papers of Na's group [48, 52–54].

2.3 Material properties and boundary conditions

The test material used in this study was SUS304 stainless steel plate with a thickness of 4 mm. The physical properties of the material considered and the coefficients used in the simulation are listed in Tab. 1.

Figure 1 shows the coordinate system and boundary types used in the numerical study. The analytical domain was set to 34 mm in length, 26 mm in width, and 4.5 mm in height including the void regions at the upper side allowed for free surface tracking. In all, 1,554,769 cells were used in the computation, and the size of the smallest cell was 0.0625 mm × 0.0625 mm × 0.0625 mm, as shown in Fig. 2.

Both the top and bottom boundaries of the computational domain were set as pressure outlet boundaries (i.e., indicated by "P" in Fig. 1), while the other four side boundaries of the computational domain were set as continuative boundaries (i.e., marked by "C" in Fig. 1). The energy on both top and bottom free surfaces was balanced between the arc heat flux, the laser heat flux, heat dissipation by convection and radiation, and the heat loss due to surface evaporation. On the vapour/liquid interface, the recoil pressure was calculated and applied to the vapour/liquid interface through a user-defined subroutine, while static pressure, dynamic pressure, surface tension, and ambient atmospheric pressure were automatically treated by FLOW3D itself.

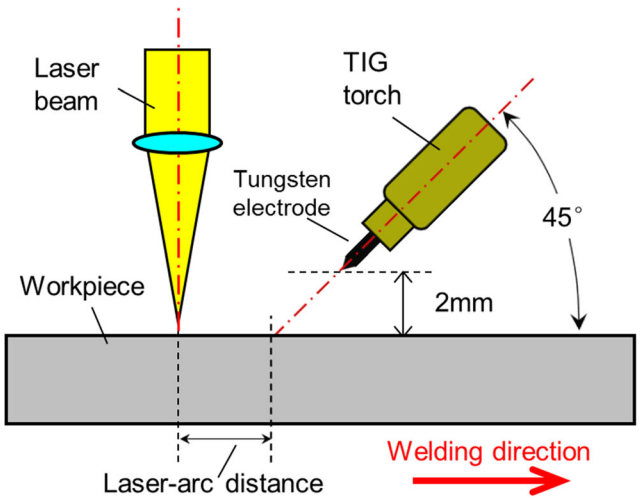

Fig. 3 Definition of the distance between the laser and the arc in hybrid welding

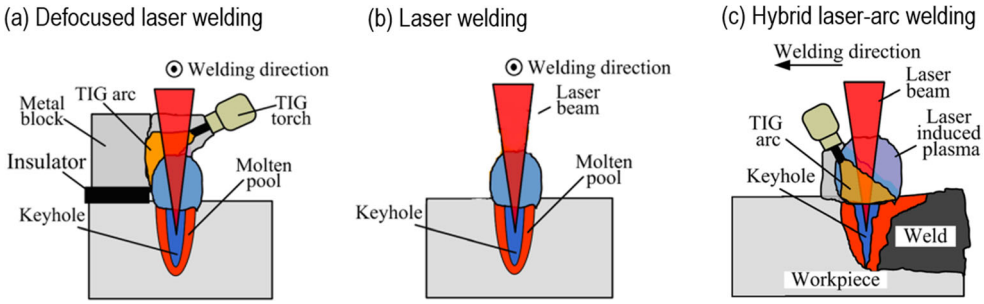

Fig. 4 Schematic of the experimental welding schemes [10]

Details of the computational procedure can be found in the previously published papers of Na's group [48, 52–54].

2.4 Process parameters

2.4.1 Parameters in experimental validation

Commercial SUS304 stainless steel rolled plates were taken as test material. The nominal chemical composition in weight percent was 19Cr, 9Ni, and balance Fe. The dimension of specimens was 150 × 100 × 4 mm.

The JHM-1GXY-400X pulsed Nd: YAG laser was used as the laser welding equipment. The laser beam was passed through a focusing lens with the diameter and focal length being 30 and 70 mm, separately, onto the surface of workpieces in a focal spot with a diameter of 0.3 mm. The hybrid laser-arc welding system consisted of a JHM-1GXY-400X pulsed Nd:YAG laser in combination with a Panasonic TX400 DC gas tungsten arc welding equipment. The angle between laser beam axis and TIG welding torch was set to be at 40. The detailed parameters in various welding processes are shown in Table 2. All samples were welded by performing the "bead on-plate" processing method to eliminate the complications from the gap variations.

2.4.2 Parameters in numerical study

Based on the established model, the laser energy coupling behaviours in three hybrid welding processes and in pure laser welding process were compared. Hereinafter, the laser-arc hybrid welding processes at the laser-arc distances of 0, 1.5, and 2.5 mm, separately, referred to these three simulations. Figure 3 shows the definition of the distance between laser and arc in hybrid welding.

2.5 Validation procedure

The principle mechanisms of the synergistic interaction between the laser and arc in hybrid welding are commonly attributed to surface heating interaction (i.e., preheating of work piece), stabilisation of the arc root, and constriction of the arc plasma column [1, 9, 12].

In present study, the pulsed laser with the average power and pulse width being 350 W and 5.5 ms, respectively, and the pulse frequency of 20 Hz was adopted. In other words, the duration of laser irradiation only accounted for about 11% of a whole pulse period and the arc was the only heat source during the remaining about 89%. Therefore, the effect of laser on the stabilisation of the arc root and constriction of the arc plasma column was greatly weakened and was neglected in all the work of this study in order to simplify the simulation process. But the thermal energy accumulation effect resulting from the overlap of the two heat sources (i.e., laser and arc) was considered in this study in a natural way.

With regard to the absorption and defocusing effects of arc plasma on the laser beam passing through the TIG arc, a comparison experiment between defocused laser beam welding and conventional pure laser beam welding was carried out previously [10]. During the defocused laser welding process, to insure that laser beam would pass through the TIG arc before it reached the work piece surface and the TIG arc did not heat the work piece, TIG arc was ignited on a laterally placed SUS304 block instead of the work piece, as shown in Fig. 4(a).

Before the established model was used to analyse both laser welding and hybrid welding processes, comparisons between simulated and experimental results were conducted for pure pulsed laser welding and hybrid welding process [10]. The

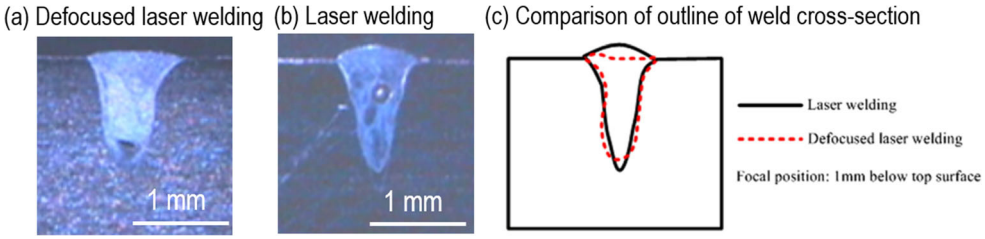

Fig. 5 Comparison of the morphology of cross-section betweendeforcused laser welding and traditional laser welding (a) deforcused laser welding (b) laser welding and (c) comparison of outline of weld crosssection

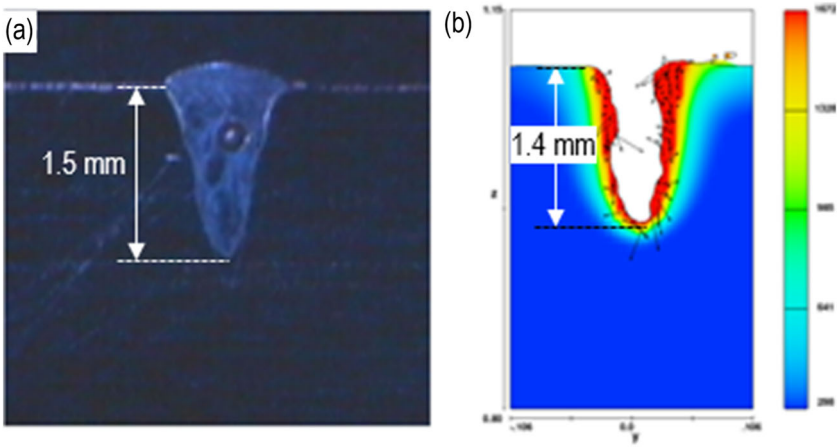

Fig. 6 Comparison of weld cross section of laser welding between **a** test result and **b** simulation result at the end of a laser pulse period [10]

schematics of laser welding and hybrid laser-arc welding are shown in Fig. 4(b, c).

3 Validation results

3.1 Interactions between sources

Figure 5 compared the weld cross section generated by traditional laser welding and defocus laser welding [10]. It can be found from Fig. 5 that difference of weld depth between defocused laser welding and laser welding was slight, which indicated that the arc plasma only had slight effect on the laser beam.

3.2 Reliability of the employed model

Figure 6 shows the experimental result of the weld cross section and simulation result at the end of a laser pulse period for laser welding [10]. As can be seen, the simulated results, especially the computed weld depth, matched the experimental results well. Figure 7 shows the experimental result of the weld cross section and simulation result at the end of a laser pulse period for hybrid laser-arc welding with zero inter-heat source distance. It can be observed that the computed weld depth matched the experimental results well whereas the computed weld width, especially on the lower part, was a little wider than the experimental one. But it was in an acceptable extent when considered the good matching of the whole profile. Based on the above considerations, the model was developed and used in all the simulation in this work.

4 Results and discussions

4.1 Results

Figure 8a shows the variation of laser energy coupling efficiencies with time in laser welding process and hybrid welding processes with various laser-arc distance. The enlarged view of the results before 0.9 ms in Fig. 8a was given in Fig. 8b.

As demonstrated in Fig. 8a, b, a common feature of the laser energy coupling behaviour of four welding processes was that laser energy coupling efficiency violently fluctuated and grew rapidly in the initial phase of a laser pulse, then

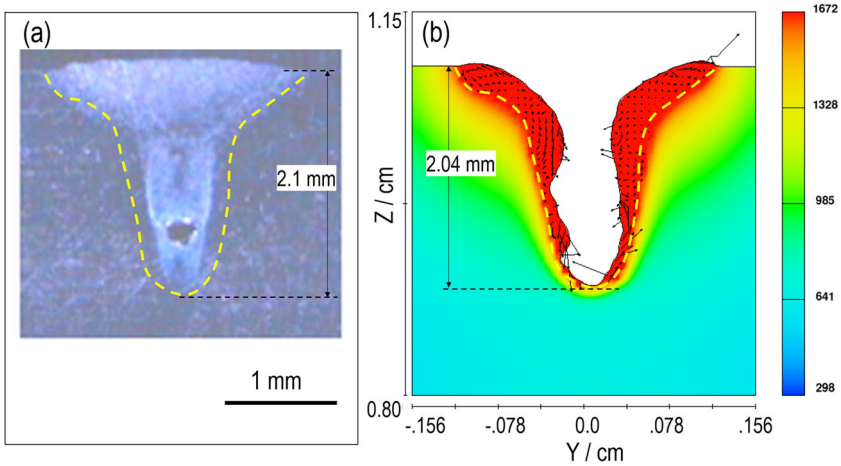

Fig. 7 Comparison of weld cross section of hybrid laser-arc welding between **a** test result and **b** simulation result at the end of a laser pulse period [10]

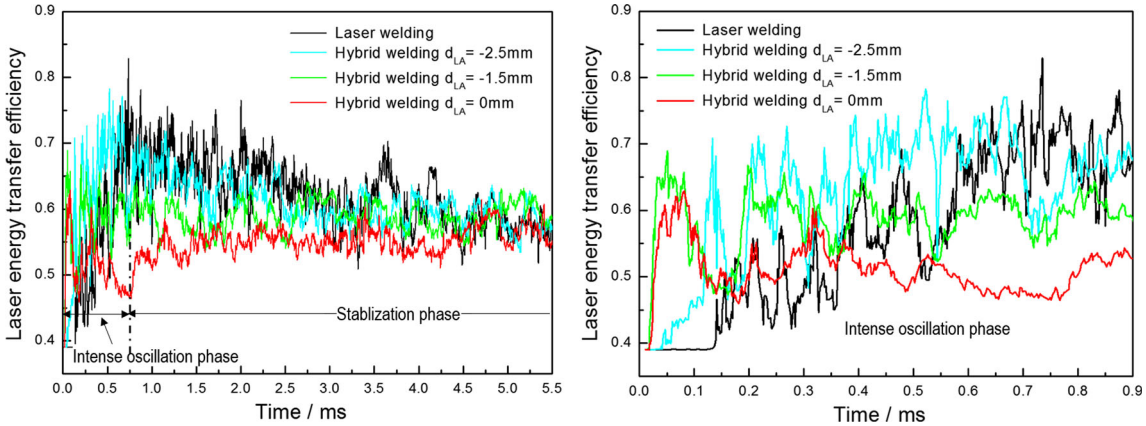

Fig. 8 Comparison of laser energy coupling efficiencies in laser welding and hybrid welding process (a) 0 ms to 5.5 ms (left) and (b) 0 ms to 0.9 ms

reduced after reaching a peak value, and finally tended to be stable. Four welding processes in decreasing order of the peak value of laser energy coupling efficiencies during a laser pulse period were laser welding, hybrid welding with a d_{LA} of 2.5 mm, hybrid welding with a d_{LA} of 1.5 mm, and hybrid welding with a d_{LA} of 0 mm.

It can be seen from Fig. 8b that the laser energy coupling efficiency was constant (i.e., about 0.39) in the initial stage of a laser pulse during various welding processes. And then, in the hybrid welding processes with d_{LA} values of 0 and 1.5 mm, the laser energy coupling efficiencies increased rapidly from about 0.02 ms onwards. It can also be found from Fig. 8b that within the initial 0.09 ms of the welding process, the laser energy coupling efficiencies in the hybrid welding processes at laser-arc distances of 0 and 1.5 mm were obviously higher than that in the other two welding processes. It can be found that the laser energy coupling efficiency in the hybrid welding process at a laser-arc distance of 0 and 1.5 mm reached about 60 and 65%, respectively. Then, the laser energy coupling efficiencies were found to decrease quickly in these two processes during the period spanning 0.1–0.15 ms and gradually tended to be stable after 1 ms. Afterwards, the laser energy coupling efficiencies in these two processes fluctuated around 55 and 60%, respectively, until the end of laser pulses, as illustrated in Fig. 8a.

In addition, it can be found in Fig. 8b that in the hybrid welding process with a d_{LA} value of 2.5 mm, the laser energy coupling efficiency was found to rise slowly from about 0.04 ms onwards, which costed about twice the time that in the hybrid welding processes where laser beams were radiated onto the surface of the molten pool (i.e., with d_{LA} values of 0 or 1.5 mm). It can be observed in Fig. 8a that the laser energy coupling efficiency in the hybrid welding process at a laser-arc distance of 2.5 mm kept increasing during the period of 0.04–0.7 ms and instantaneously reached its peak of 78% at about 0.7 ms. This peak value was higher than those in the welding processes with d_{LA} values of 0 or 1.5 mm. The duration of the growth of laser energy coupling efficiency and peak coupling efficiency were about 10 times and about 1.2 times, of those in the hybrid welding process where d_{LA} was 0 mm, respectively. During the period from 0.7 to 2.5 ms, the laser energy coupling efficiency in this process (i.e., d_{LA} value of 2.5 mm) continued to decrease and gradually tended to be stable after 2.5 ms. Afterwards, the laser energy coupling efficiency of this process fluctuated in the vicinity of 60% until the end of the laser pulses.

In the case of pure laser welding, the laser energy coupling efficiency continued to grow during the period from 0.14 to 0.72 ms and then reached its peak of approximately 85% at about 0.72 ms, as shown in Fig. 8a. Afterwards, the laser energy coupling efficiency in the pure laser welding process decreased from 0.72 to 3.2 ms and then tended to be stable after 3.2 ms and fluctuated in the vicinity of 60% until the end of the laser pulses.

Figure 9 shows the total laser energy coupling efficiencies during a laser pulse period in four welding processes. As can be seen, the total laser energy coupling efficiency was the

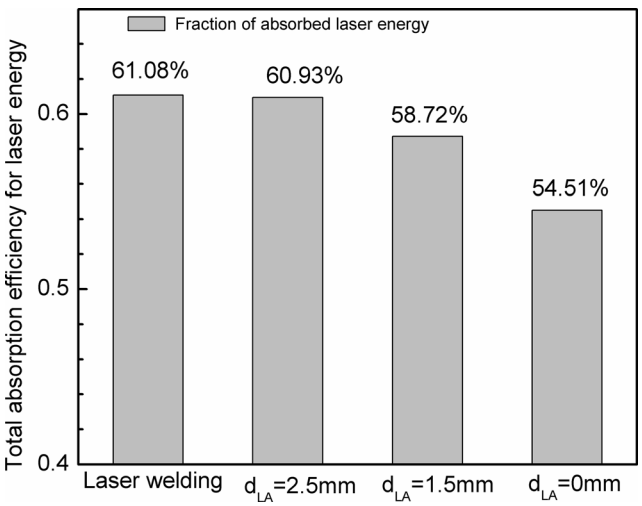

Fig. 9 Total laser energy coupling efficiencies during a laser pulse period

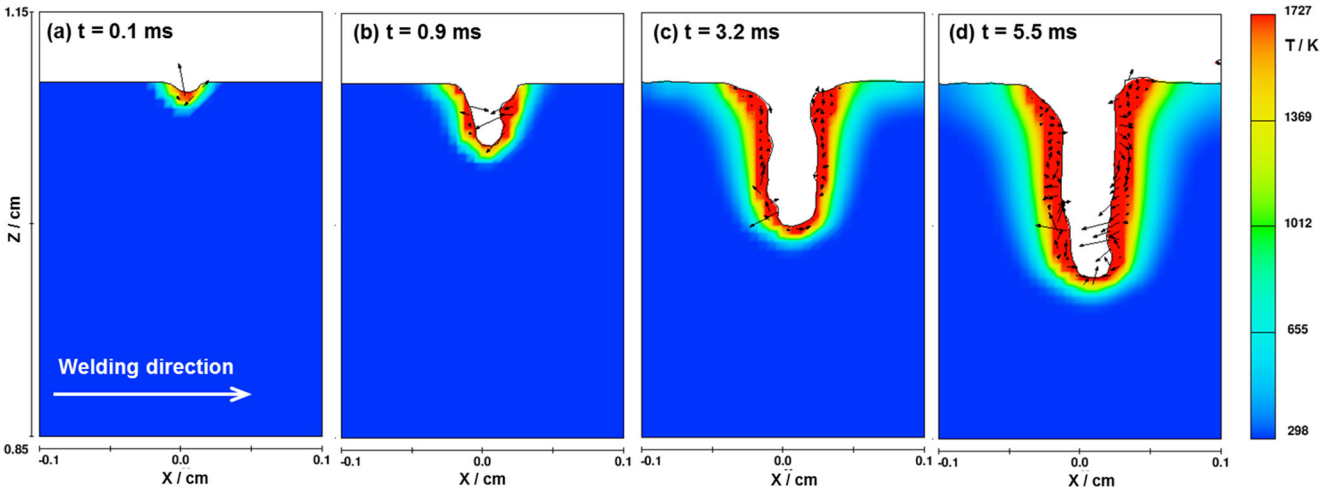

Fig. 10 Temperature fields and the morphologies of keyholes and molten pools on longitudinal sections during a laser pulse period in the laser welding process

highest in pure laser welding process where about 61.1% of laser energy was absorbed by workpieces. In addition, the hybrid welding process where d_{LA} was 2.5 mm showed the second highest laser energy coupling efficiency, that was, 60.9% of laser energy was absorbed by the workpieces. The lowest laser energy coupling efficiency was found in the hybrid welding process at a laser-arc distance of 0 mm where merely 54.5% of the laser pulse energy was shown to be absorbed by the workpieces. This value was about 6.5% lower than that in the hybrid welding process where d_{LA} was 2.5 mm. The similar results were reported by Zhang W et al. in CO_2 laser-pulsed GMAW hybrid welding process based on spectral diagnosis technique. They found that the laser energy absorption decreased from 94.16% for laser welding to 85.84% for hybrid welding [20].

4.2 Discussion

4.2.1 Occurrence of laser beam multiple reflection

In this study, the temperature dependency of the absorption factor of metal for laser irradiation was neglected. Therefore, the laser energy coupling efficiency was constant (i.e., about 0.39) in the initial stage of a laser pulse during various welding processes, which implied that laser beam was reflected only one time, as shown in Fig. 8b. After that, laser energy coupling efficiency climbed sharply in various welding processes, which undoubtedly indicated the formation of keyhole in molten pool and the occurrence of laser beam multiple reflection within the keyhole. According to Fig. 8, laser beam multiple reflection occurred at about 0.02 ms in the hybrid welding processes with d_{LA} values of 0 and 1.5 mm. In the hybrid welding process with a d_{LA} value of 2.5 mm, laser beam multiple reflection occurred at about 0.04 ms, which costed about twice the time that in the hybrid welding processes where laser beams were radiated onto the surface of the molten pool (i.e., with d_{LA} values of 0 or 1.5 mm). The laser irradiation time needed for the occurrence of multiple reflections of laser beams was about seven times of that in hybrid welding processes with d_{LA} values of 0 or 1.5 mm. This phenomenon could be understood as that initial temperature of the material irradiated by laser beam was different in various welding processes.

4.2.2 Evolution history of keyhole depth and its influence

The difference in laser energy coupling behaviour in these four welding processes could be related to that of the evolution

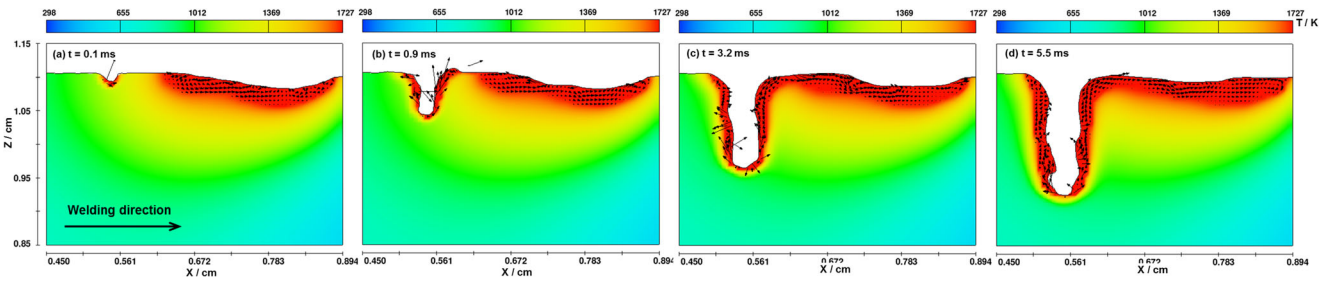

Fig. 11 Temperature fields and the morphologies of keyholes and molten pools on longitudinal sections during a laser pulse period in the hybrid welding process at a laser-arc distance of 2.5 mm

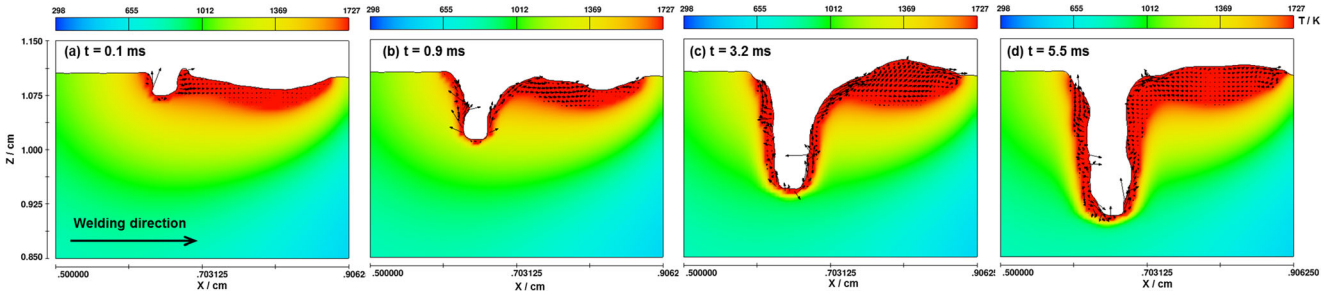

Fig. 12 Temperature fields and the morphologies of keyholes and molten pools on longitudinal sections during a laser pulse period in the hybrid welding process at a laser-arc distance of 1.5 mm

of keyhole depth in the welding processes under different conditions. Figure 10 depicts the variations of temperature fields and the morphologies of keyholes and molten pools on longitudinal sections during a laser pulse period in the pure laser welding process, while the simulated results on longitudinal sections during a laser pulse period in hybrid welding processes at laser-arc distances of 2.5, 1.5, and 0 mm are shown in Figs 11, 12, and 13, respectively. The dynamic variations in keyhole depth in these four welding processes during a laser pulse period are illustrated in Fig. 14.

To begin with, the morphologies of keyholes during the initial phases of laser pulse in the four welding processes were compared. According to Figs 10, 11, 12, 13, and 14, during the initial phases of the welding processes at laser-arc distances of 0 and 1.5 mm, keyholes were formed at a faster speed than those in the other two processes, that is, hybrid welding with a d_{LA} value of 2.5 mm and pure pulsed laser welding. Meanwhile, it was found that the keyhole depth increased at the fastest speed in the hybrid welding process at a laser-arc distance of 0 mm, followed by that in the hybrid welding process with a d_{LA} value of 1.5 mm, as shown in Fig. 14b. At a d_{LA} value of 2.5 mm, laser beam was emitted so as to irradiate outside the molten pool. In the pure laser welding process, laser beam irradiated the surface of metal which had not been pre-heated. Therefore, the growth rates of keyhole depth in hybrid welding with a d_{LA} value of 2.5 mm and pure pulsed laser welding would significantly decrease. The larger the keyhole depth, the more conducive it was to the occurrence of multiple reflections of the laser beam in keyholes and the transfer of laser energy into the workpieces. Therefore, during the initial phases (0.02 to 0.09 ms) in the welding processes, where the laser beam directly irradiated the surface of the molten pool (i.e., d_{LA} values of 0 and 1.5 mm, respectively), the energy coupling efficiencies were shown to be high, while those in the hybrid welding process with a d_{LA} value of 2.5 mm and pure laser welding process were found to be low (see Fig. 8b).

4.2.3 Evolution history of keyhole diameter and its influence

Figure 15 shows the simulated results of velocity vectors along the *x*-direction and the calculated results concerning the diameters of keyholes in the four welding processes at 0.1 ms. Based on Fig 15c, d, in the hybrid welding processes at laser-arc distances of 1.5 and 0 mm separately, laser beams directly irradiated the surface of the liquid metal and therefore the deep keyholes were generated at 0.1 ms. In addition, it can also be found from Fig. 15d that, in the hybrid welding process with a d_{LA} value of 0 mm, the liquid metal in the front of keyholes flowed along the positive direction of the *x*-axis under the effect of the recoil pressure acted on keyhole wall at 0.1 ms, while the liquid metal in the back of keyholes flowed in the opposite direction. As a result, the diameter of the keyholes was significantly increased. According to Fig. 15c, in the hybrid welding process with a d_{LA} value of 1.5 mm, little liquid metal was found in the back of the keyholes at 0.1 ms. Nevertheless, as the liquid metal in the front of keyholes flowed along the positive direction of the *x*-axis under the effect of the recoil pressure, the diameter of keyholes in this process was also increased. In these two processes,

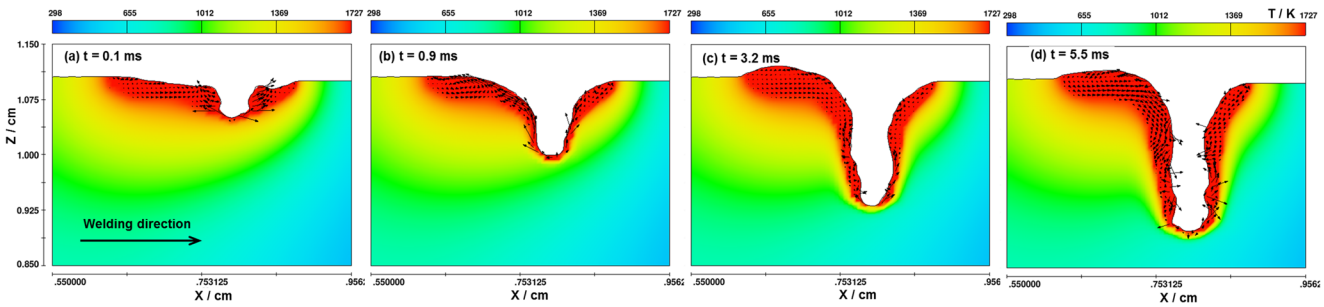

Fig. 13 Temperature fields and the morphologies of keyholes and molten pools on longitudinal sections during a laser pulse period in the hybrid welding process at a laser-arc distance of 0 mm

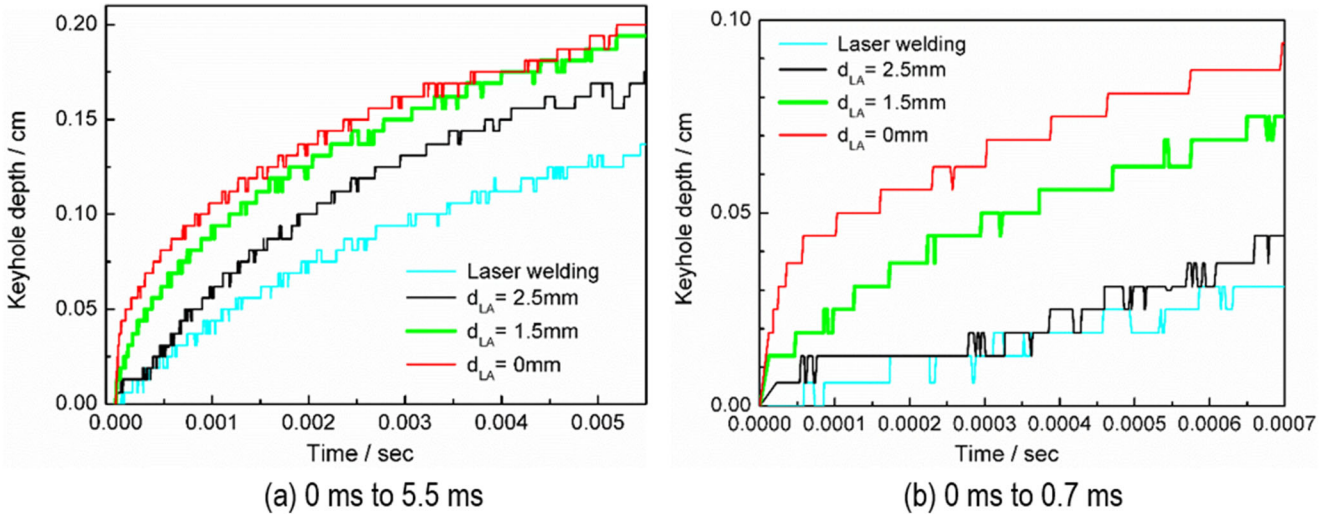

Fig. 14 Fig. 14 Dynamic variation of the keyhole depth with time during a laser pulse period (a) 0 ms to 5.5 ms and (b) 0 ms to 0.7 ms

the significant growth in the radius of the keyholes led to a decreasing depth–width ratio. According to Kaplan's computational results, the number of reflections would greatly decreased with the decreasing of depth–width ratio [55], and the same results have been obtained in previous study [36]. As a consequence, the laser energy coupling

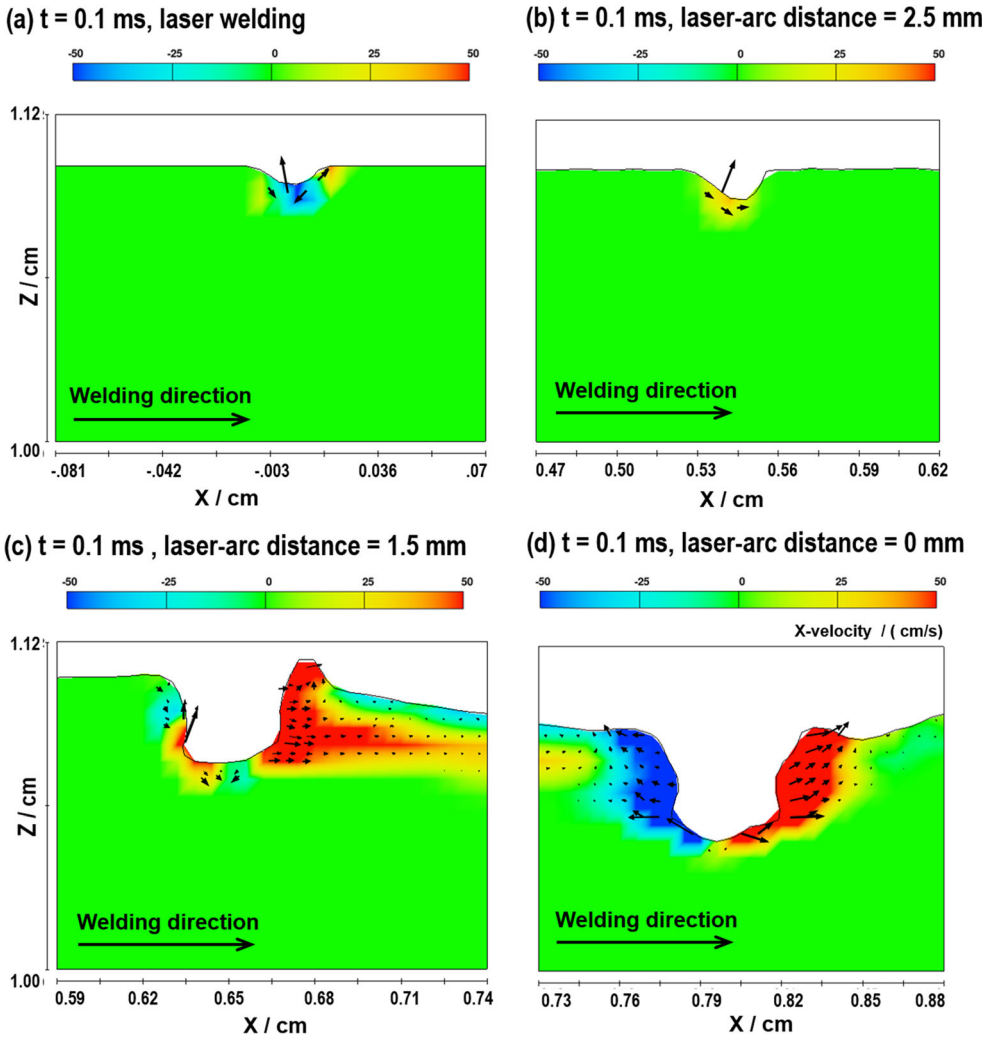

Fig. 15 Cloud pictures of calculated velocity vectors in the *x*-direction at 0.1 ms in four different welding processes

efficiencies in these two welding processes rapidly decreased from about 0.09 ms.

Figure 16 shows the simulated results of velocity vectors in the *x*-direction and the calculated results regarding the morphologies of keyholes in four different welding processes at 0.9 ms. The laser-arc distance affected not only the keyhole depth but also the shape of the front and back walls of the keyholes. As seen in Fig. 16, in the welding process at a d_{LA} value of 0 mm, the front wall of the keyholes was inclined forward, while the back wall sloped in the opposite direction. Consequently, the diameter of keyhole orifice was increased significantly. In the welding process at a laser-arc distance of 1.5 mm, the back wall of the keyholes was approximately vertical, while the front wall was inclined forward so that same increase could also be found in the diameter of keyhole orifice. In contrast, the diameters of keyhole orifice at 0.9 ms in the hybrid welding process at a d_{LA} value of 2.5 mm and the pure laser welding process were smaller, as shown in Fig 16a, b. As a result, the laser energy coupling efficiencies in these two processes were higher at 0.9 ms, as shown in Fig. 8.

As shown in Fig. 8, during the period from 0.9 to 3.2 ms, both the laser energy coupling efficiencies in the hybrid welding process at a laser-arc distance of 2.5 mm and pure laser welding process were found to continuously decrease. Figure 17a, b shows the morphologies of keyholes at different moments in the hybrid welding processes at d_{LA} values of 2.5 and 0 mm, separately. As can be seen, when laser beam was irradiated upon outside the molten pool (i.e., d_{LA} was 2.5 mm), the diameter of keyholes at 3.2 ms was greater than that at 0.9 ms. With increasing keyhole diameter, the reflection times of laser beams in a keyhole of unit depth would decrease, which went against the absorption of laser energy by keyhole wall. However, when laser beam was radiated onto the surface of the molten pool (i.e., d_{LA} was 0 mm), a slight difference was found between the diameters of keyholes at 3.2 and 0.9 ms. In addition, as the laser pulses continued, the volume of liquid metal around the keyholes continuously increased in the hybrid welding process at a d_{LA} value of 2.5 mm and in the pure laser welding process. This was bound to enhance the instability of keyholes (as shown in Fig. 18) and gave rise to the reducing of laser energy coupling efficiency. Therefore, during the period from 0.9 to 3.2 ms, the laser energy coupling efficiencies in these two processes continued to decrease. After about 3.2 ms, the laser energy coupling efficiencies gradually tended to be stable.

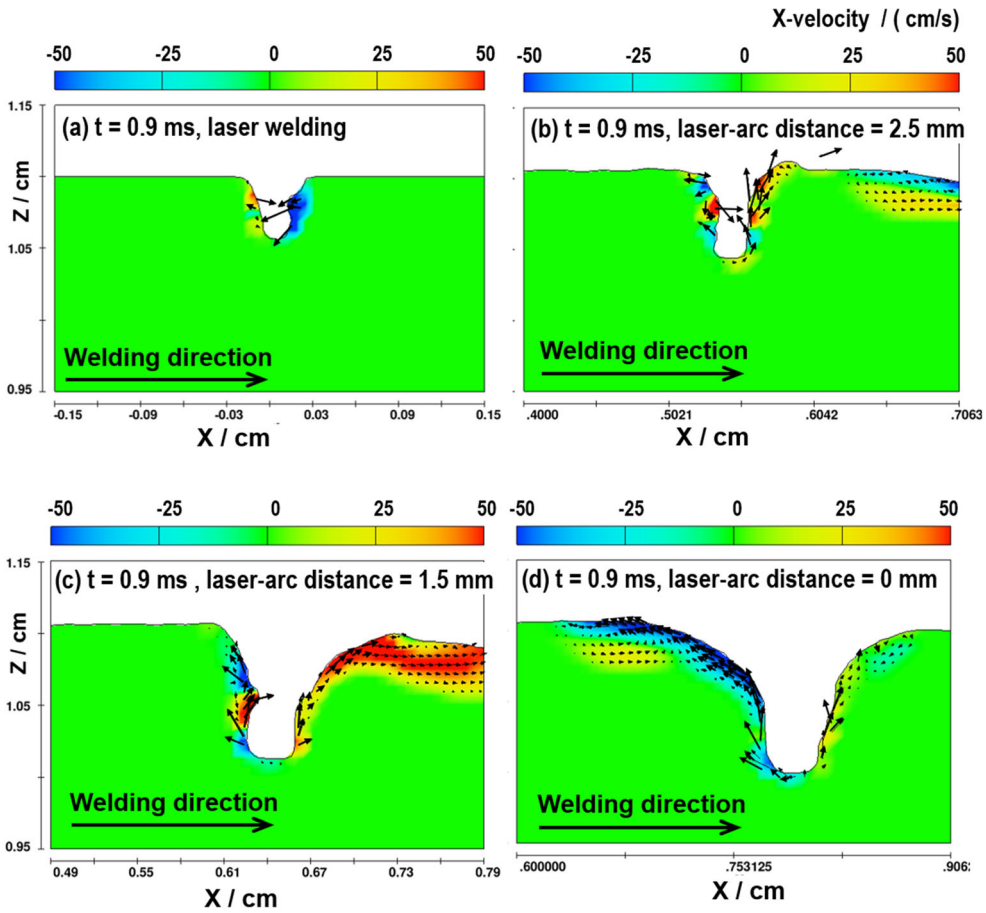

Fig. 16 Cloud pictures of calculated velocity vectors in the *x*-direction at 0.9 ms in four different welding processes

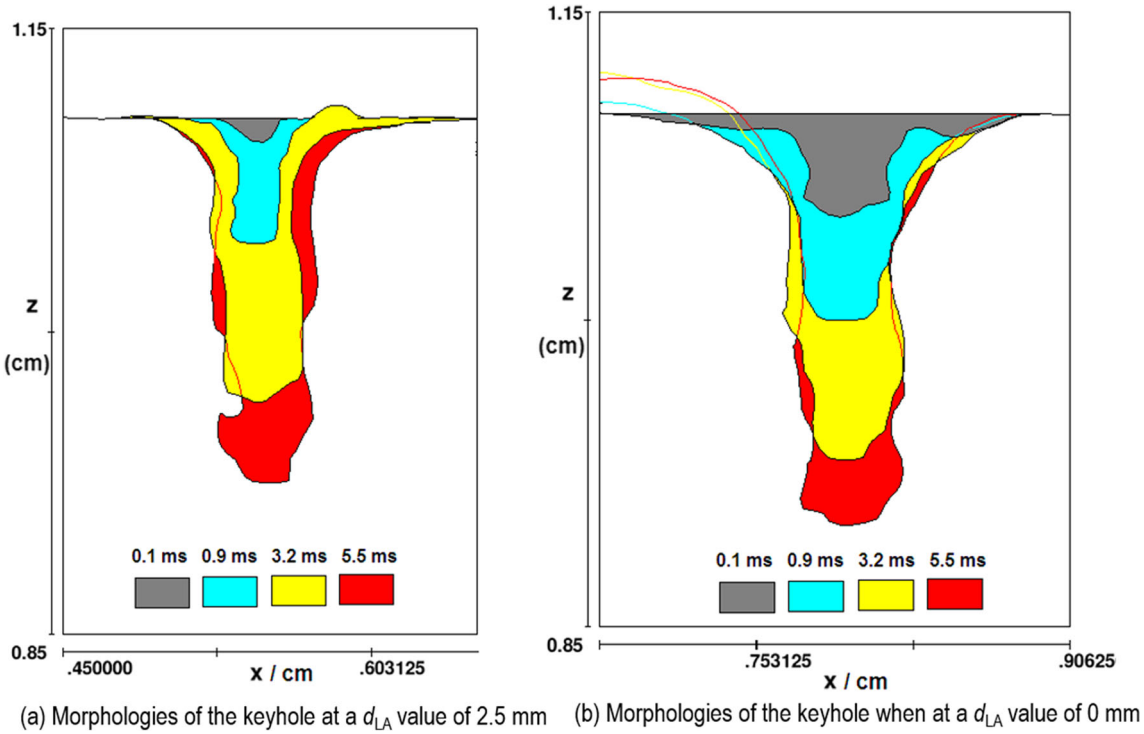

(a) Morphologies of the keyhole at a d_{LA} value of 2.5 mm (b) Morphologies of the keyhole when at a d_{LA} value of 0 mm

Fig. 17 Morphologies of keyholes at different times

5 Conclusions

1. The occurrence of multiple reflections of laser beam in keyhole was the key point of the increasing of laser energy coupling efficiency. Once forming the multiple reflections, the laser energy coupling efficiency would grow rapidly in the initial phase of laser pulse, then reduce after reaching a peak value, and finally tend to be stable.
2. In the hybrid welding process where laser beam was radiated onto the surface of the molten pool, the laser irradiation time needed for the occurrence of multiple reflections of laser beams was about 0.02 ms (d_{LA} = 0 and d_{LA} = 1.5), which was half of that in the hybrid welding process with a d_{LA} of 2.5 mm and one seventh of that in the pure laser welding process.
3. The larger the laser-arc distance, the longer the growth phase of laser energy coupling efficiency lasted and therefore the larger the peak coupling efficiency. The duration of the growth of laser energy coupling efficiency and peak coupling efficiency in the hybrid welding process at a laser-arc distance of 2.5 mm were about 10 times, and about 1.2 times, of those in the hybrid welding process where d_{LA} was 0 mm, respectively.
4. The four welding processes, in decreasing order of total laser energy coupling efficiencies during a laser pulse period, were pure laser welding, and then hybrid welding process where laser beam was irradiated upon the surface of the solidified weld metal in the back of the molten pool, upon the rear part of the molten pool surface, and upon the centre of the molten pool surface.

Fig. 18 Examples of keyhole instability

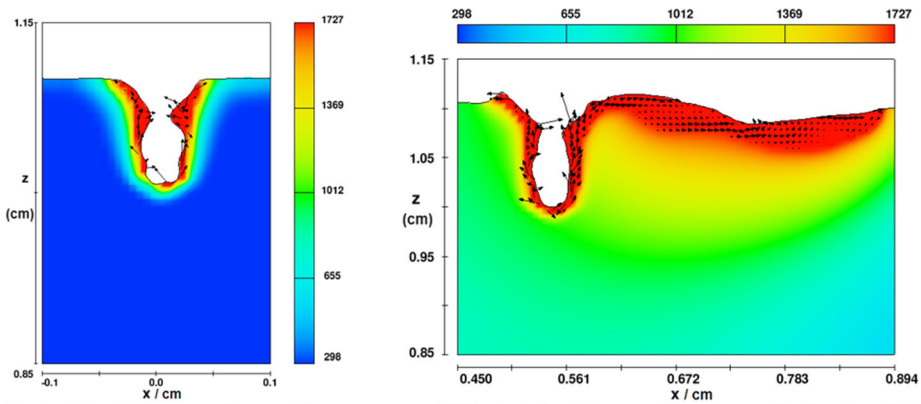

(a) The keyhole at 2.7 ms: purelaser welding process (b) The keyhole at 2 ms: welding process at a d_{LA} value of 2.5 mm

5. In the hybrid welding process, the smaller the laser-arc distance, the faster the growth rate of keyhole depth during a laser pulse period, the larger the maximum keyhole depth formed by each laser pulse. However, the smaller the laser-arc distance, the farther the keyhole wall moved backward along the radial direction of the keyholes under the effect of recoil pressure, the larger the keyhole diameter. And the significantly increasing keyhole diameter impaired the ability to produce multiple reflections of the laser beams in the keyholes. Finally, the total laser energy coupling efficiencies during a laser pulse period reduced with the decrease in the laser-arc distance.

Acknowledgement This work was supported by the National Natural Science Foundation of China (Grant No. 51275391) and BK21 program of Korea, Mid-career Researcher Program through NRF (Grant No. 2013R1A2A1A01015605).

References

1. Steen WM (1980) Arc augmented laser processing of materials. J Appl Phys 51:5636–5641
2. Yan J, Gao M, Li G, Zhang C, Zeng X, Jiang M (2012) Microstructure and mechanical properties of laser-MIG hybrid welding of 1420 al-li alloy. Int J Adv Manuf Technol 66(9–12): 1467–1473
3. Li C, Liu L (2012) Investigation on weldability of magnesium alloy thin sheet t-joints: arc welding, laser welding, and laser-arc hybrid welding. Int J Adv Manuf Technol 65(1–4):27–34
4. Hu B, Richardson IM (2007) Microstructure and mechanical properties of AA7075(T6) hybrid laser/GMA welds. Mater Sci Eng A 459(1–2):94–100
5. Xu GX, Wu CS, Qin GL, Wang XY, Lin SY (2011) Adaptive volumetric heat source models for laser beam and laser + pulsed GMAW hybrid welding processes. Int J Adv Manuf Technol 57(1–4):245–255
6. Liu LM, Wang JF, Song G (2004) Hybrid laser-TIG welding, laser beam welding and gas tungsten arc welding of AZ31B magnesium alloy. Mater Sci Eng A 381(1–2):129–133
7. Hu B, den Ouden G (2005a) Laser induced stabilisation of the welding arc. Sci Technol Weld Joi 10(1):76–81
8. Li R, Yu J, Sun R, Mi G, Wang C, Shao X (2016) A study of droplet transfer behavior in ultra-narrow gap laser arc hybrid welding. Int J Adv Manuf Technol:1–12
9. Hu B, Den Ouden G (2005b) Laser-induced stabilisation of the welding arc. Sci Technol Weld Join 10(1):76–81
10. Zhang L, Gao X, Sun M, Zhang J (2014a) Weld outline comparison between various pulsed Nd: YAG laser welding and pulsed Nd: YAG laser–TIG arc welding. Int J Adv Manuf Technol 75(1–4): 153–160
11. Zhang LJ, Ning J, Zhang XJ, Zhang GF, Zhang JX (2015) Single pass hybrid laser-MIG welding of 4 mm thick copper without preheating. Mater Des 74:1–18
12. Hu B, Ouden G (2005) Synergetic effects of hybrid laser/arc welding. Sci Technol Weld Join 10:427–431
13. Kozakov R, Gött G, Uhrlandt D, Emde B, Hermsdorf J, Wesling V (2015) Study of laser radiation absorption in a TIG welding arc. Welding in the World Le Soudage Dans Le Monde 59(4):1–7
14. Fuerschbach PW, Eisler GR (2002) Effect of laser spot weld energy and duration on melting and absorption. Science and Technology of Welding & Joining 7:241–246
15. Fuerschbach PW (1996) Measurement and prediction of energy transfer efficiency in laser beam welding. Weld J 75(1):S24–S34
16. Jouvard JM, Girard K, Perret O (2001) Keyhole formation and power deposition in Nd:YAG laser spot welding. Journal of Physics D Applied Physics 34(18):2894–2901(8)
17. Hu B, Hu S, Shen J, Li Y (2015) Modeling of keyhole dynamics and analysis of energy absorption efficiency based on Fresnel law during deep-penetration laser spot welding. Comput Mater Sci 97: 48–54
18. Kaplan AFH (2013) Laser absorptivity on wavy molten metal surfaces: categorization of different metals and wavelengths. Journal of Laser Application 26(1):012007
19. Weston J (2000) Surface related features of laser welding of aluminium alloys. ISIJ Int 40:S6–S9
20. Zhang W, Fang LI, Min LI, Hua XM, Cai Y (2016) Study of the laser absorption characteristics of CO_2 laser-pulsed GMAW hybrid welding based on spectral diagnosis technique. Spectroscopy & Spectral Analysis 36(4):931–918
21. Greses J, Barlow CY, Hilton PA, Steen WM (2003) Effects of different gas environments on CO_2 and Nd:YAG laser welding process efficiencies. Proceedings of SPIE - The International Society for Optical Engineering 4831:257–262
22. Matsuda J, Utsumi A (1988) TIG or MIG arc augmented laser welding of thick mild steel plate. Joining and Materials, July 1988:31–34
23. Katayama S, Uchiumi S, Mizutani M, Wang J, Fujii K (2007) Penetration and porosity prevention mechanism in YAG laser-MIG hybrid welding. Weld Int 21(1):25–31
24. Liu LM, Yuan ST, Li CB (2012) Effect of relative location of laser beam and TIG arc in different hybrid welding modes. Sci Technol Weld Joi 17(6):441–446
25. Andersen M, Jensen A (2001) 'Hybrid Nd:YAG laser MIG welding in aluminium', in Olsen F and Kristensen J, Proc. 8th Nordic Conference on Laser Materials Processing, Lyngby, Denmark, 371–380
26. Uchiumi S, Wang JB, Katayama S, Mizutani M, Hongu T, Fujii K (2004) Penetration and welding phenomena in YAG laser -MIG hybrid welding of aluminum alloy. ICALEO 2004 Congress Proceedings, San Francisco, LIA, 97, P530.(CD)
27. Moradi M, Ghoreishi M, Frostevarg J, Kaplan AFH (2013) An investigation on stability of laser hybrid arc welding. Opt Laser Eng 51(4):481–487
28. Song G, Liu L, Wang P (2006) Overlap welding of magnesium AZ31B sheets using laser-arc hybrid process. Mater Sci Eng A 429(1):312–319
29. Kim C, Choi W, Kim J, Rhee S (2008) Relationship between the weldability and the process parameters for laser-TIG hybrid welding of galvanized steel sheets. Mater Trans 49(1):179–186
30. Abe N, Kunugita Y, Hayashi M, Tsuchitani Y (1997) Dynamic observation of high speed laser-arc combination welding of thick steel plates (physics, processes, instruments & measurements). Trans JWRI 26(2):7–11
31. Ribic B, Burgardt P, DebRoy T (2011) Optical emission spectroscopy of metal vapor dominated laser-arc hybrid welding plasma. J Appl Phys 109(8):083301
32. Kiran DV, Na SJ (2014) Numerical studies on submerged arc welding process. Journal of Welding and Joining 32(4):1–9
33. Kiran DV, Cho DW, Lee HK, Kang CY, Na SJ (2014) A study on the quality of two-wire tandem submerged arc welds under iso-heat input conditions. Int J Adv Manuf Technol 78(1–4):53–62
34. Kiran DV, Cho DW, Song WH, Na SJ (2015) Arc interaction and molten pool behavior in the three wire submerged arc welding process. Int J Heat Mass Transf 87:327–340

35. Kiran DV, Cheon J, Arif N, Chung H, Na SJ (2016) Three-dimensional finite element modeling of pulsed AC gas metal arc welding process. Int J Adv Manuf Technol:1–22. doi:10.1007/s00170-015-8297-2
36. Zhang LJ, Zhang JX, Gumenyuk A, Rethmeier M, Na SJ (2014b) Numerical simulation of full penetration laser welding of thick steel plate with high power high brightness laser. J Mater Process Technol 214(8):1710–1720
37. Cheon J, Kiran DV, Na SJ (2016a) Thermal metallurgical analysis of GMA welded AH36 steel using CFD-FEM framework. Mater Des 91:230–241
38. Cheon J, Kiran DV, Na SJ (2016b) CFD based visualization of finger shaped evolution in gas metal arc welding process. Int J Heat Mass Transf 97:1–14
39. Wu L, Cheon J, Kiran DV, Na SJ (2016) CFD simulations of GMA welding of horizontal fillet joint based on coordinate rotation of arc models. J Mater Process Technol 231:221–238
40. Pang S, Chen X, Shao X, Gong S, Xiao J (2016a) Dynamics of vapor plume in transient keyhole during laser welding of stainless steel: local evaporation, plume swing and gas entrapment into porosity. Opt Laser Eng 82:28–40
41. Pang S, Shao X, Li W, Chen X, Gong S (2016b) Dynamic characteristics and mechanisms of compressible metallic vapor plume behaviors in transient keyhole during deep penetration fiber laser welding. Appl Phys A Mater Sci Process 122(7):1–18
42. Pang S, Chen X, Li W, Shao X, Gong S (2016c) Efficient multiple time scale method for modeling compressible vapor plume dynamics inside transient keyhole during fiber laser welding. Opt Laser Technol 77:203–214
43. Pang S, Chen X, Zhou J, Shao X, Wang C (2015) 3D transient multiphase model for keyhole, vapor plume, and weld pool dynamics in laser welding including the ambient pressure effect. Opt Laser Eng 74:47–58
44. Pang S, Chen W, Zhou J, Liao D (2014) Self-consistent modeling of keyhole and weld pool dynamics in tandem dual beam laser welding of aluminum alloy. J Mater Process Technol 217:131–143
45. Cho YT, Cho WI, Na SJ (2011) Numerical analysis of hybrid plasma generated by Nd: YAG laser and gas tungsten arc. Opt Laser Technol 43(3):711–720
46. Piekarska W, Kubiak M (2011) Three-dimensional model for numerical analysis of thermal phenomena in laser–arc hybrid welding process. Int J Heat Mass Transf 54(23):4966–4974
47. Bendaoud I, Matteï S, Cicala E, Tomashchuk I, Andrzejewski H, Sallamand P, Mathieu A, Bouchaud F (2014) The numerical simulation of heat transfer during a hybrid laser–MIG welding using equivalent heat source approach. Opt Laser Technol 56:334–342
48. Cho WI, Na SJ, Cho MH, Lee JS (2010) Numerical study of alloying element distribution in CO2 laser–GMA hybrid welding. Comp Mater Sci 49(4):792–800
49. Zhou J, Tsai HL (2009) Investigation of mixing and diffusion processes in hybrid spot laser–MIG keyhole welding. J Phys D Appl Phys 42(9):095502
50. Ribic B, Rai R, DebRoy T (2008) Numerical simulation of heat transfer and fluid flow in GTA/laser hybrid welding. Sci Technol Weld Joi 13(8):683–693
51. Flow Science, I, 2008. FLOW 3D User Manual V9.2
52. Cho JH, Na SJ (2006) Implementation of real-time multiple reflection and Fresnel absorption of laser beam in keyhole. J Phys D Appl Phys 39:5372
53. Cho JH, Na SJ (2009) Three-dimensional analysis of molten pool in GMA-laser hybrid welding. Weld Joi 88:35–43
54. Cho WI, Na SJ, Thomy C, Vollertsen F (2012) Numerical simulation of molten pool dynamics in high power disk laser welding. J Mater Process Technol 212:262–275
55. Kaplan A (1994) A model of deep penetration laser welding based on calculation of the keyhole profile. J Phys D Appl Phys 27(9):1805–1814